applied sciences

MDPI

Article

Influence of Carbon Uniformity on Its Characteristics and Adsorption Capacities of CO_2 and CH_4 Gases

Ahmed Awadallah-F [†] and Shaheen A. Al-Muhtaseb *

Department of Chemical Engineering, Qatar University, Doha P.O. Box 2713, Qatar; ahmed.awadallah@qu.edu.qa
* Correspondence: s.almuhtaseb@qu.edu.qa; Tel.: +974-4403-4139; Fax: +974-4403-4131
† On leave from the Radiation Research of Polymer Department, National Centre for Radiation Research and Technology, Atomic Energy Authority, P.O. Box 29, Nasr City, Cairo, Egypt.

Abstract: Activated carbons of resorcinol-formaldehyde aerogels (AC-RFA) were prepared and mixed with multiwall carbon nanotubes (MWCNTs) with various ratios. Samples were characterized by different techniques. The novelty of the study is in evaluating the effect of uniformity of carbon nanocomposites on their performance for the adsorption of CH_4 and CO_2 gases as well predicting the separation of their mixtures. The results indicated that, by increasing the percentage of MWCNTs into the sample, its structural uniformity and order ascend. The capacities of CH_4 and CO_2 by adsorption were measured at various temperatures, and were correlated with the extended dual site Langmuir (DSL) model. Overall, results showed that the adsorption capacity of MWCNTs towards gases is relatively very low compared to that of activated carbons. The DSL model was utilized to forecast the separation of the binary CO_2/CH_4 mixed gas based on knowledge of single component adsorption isotherm parameters. Adsorption equilibrium data of the CO_2/CH_4 binary gas mixture was forecasted at different temperatures by DSL model in accordance with the perfect-negative (PN) or perfect-positive (PP) behaviors on the heterogeneous surface of the adsorbent.

Keywords: carbon aerogel; MWCNTs; adsorption; carbon dioxide; methane; selectivity

Citation: Awadallah-F, A.; Al-Muhtaseb, S.A. Influence of Carbon Uniformity on Its Characteristics and Adsorption Capacities of CO_2 and CH_4 Gases. *Appl. Sci.* **2021**, *11*, 265. https://doi.org/10.3390/app11010265

Received: 17 March 2020
Accepted: 8 April 2020
Published: 29 December 2020

1. Introduction

Methane (CH_4) and carbon dioxide (CO_2) gases coexist often in nature, forming gas mixtures, such as natural gas, biofuel gas, landfill gas, coal bed methane, etc. [1–5]. Separation of CO_2 gas from CO_2/CH_4 mixed binary gas is a core and strategic target in enhancing the gas purity and efficiency. The existence of CO_2 impurity within CH_4 gas reduces its heating value and leads to pipeline corrosion, especially if moisture is found [6]. Furthermore, CO_2 and CH_4 gases are key players in the amassing of greenhouse gases, and subsequently in the augmented global warming crisis [7]. The greenhouse warming impact of CH_4 is 21 times bigger than that of CO_2 [8]. Owing to the strong augmentation in the cost of oil and recent rigorous ecological regulations, there is a noticeable rise in the extraction of natural gas as a strong competent source of energy [9]. Therefore, it is desired to establish efficient techniques for removing CO_2 gas from natural gas.

The separation of CO_2 gas from natural gas or biogas mixtures is of a vital importance to their economic value, and is an issue of dire investigations [10,11]. It is reported that that natural gas is principally formed from CH_4 (95%) and C_2H_6 (5%) while the biogas mainly includes CH_4 (45% to 65%) and CO_2 (30% to 40%). The higher content of CO_2 (30% to 40%) contributes to the much lower energy of biogas comparing to the natural gas [12].

The separation of CO_2 from gas mixtures is conducted by numerous techniques, such as cryogenic distillation, absorption, membrane technology, and adsorption [13]. The use of adsorption is of strategic importance in industry. Numerous materials (e.g., carbons [14,15], zeolites [8,16], metal organic frameworks [17,18], molecular sieves [19,20], and clays [21]) have attracted attention as adsorbents to separate mixtures of CO_2 and CH_4 gases. The distinguished selectivity is the most important and unique feature of adsorption processes over other separation techniques. The informative knowledge of pure and multi-component adsorption equilibrium data is necessary for designing and optimizing industrial units, and is very pivotal for determining the selectivity and the adsorption capability of specific adsorbents [6]. Nonetheless, binary or multicomponent adsorption experiments are very difficult and time-expensive. Thus, it would be advantageous if such findings could be forecasted using the traditional adsorption models. For its simplicity, the extended dual site Langmuir (DSL) model is commonly used to forecast the mixed gas adsorption equilibrium data from single component adsorption data [22–24].

Carbon nanotubes (CNTs) have attracted much attention as a result of their distinct chemical and physical properties [25,26]. CNTs are one-dimensional nanoscale substances formed of carbon atoms, where each carbon atom is sp^2 hybrid, and is bonded covalently to three adjacent carbon atoms. Upon the number of their wall layer(s), CNTs can be classified as either single-walled carbon nanotubes (SWCNTs) or multiwall carbon nanotubes (MWCNTs) [27]. It is well-known that the activated carbons are featured with disorder and non-uniformity, while MWCNTs are featured with highly uniform and ordered structures. It is expected that the structure uniformity of MWCNTs may be affected when mixing them with activated carbon nanoparticles, which reflects their changing performance in gas adsorption or separation processes. It is well-known that CNTs are very weak in adsorption capacity; therefore, the addition of other carbon materials may enhance their adsorption performance. In addition, according to the authors' knowledge, there is no work available in the literature to address the carbon–carbon interactions effect on adsorption. Consequently, this work tackles a novel issue and adds value to literature that may open new gates of research for this kind of work and reflect on properties for a wide range of related applications. Therefore, authors believe that this concept of carbon–carbon interaction is novel and needs further investigation by the research community to deduce and extract an integral vision of the reaction mechanism and its reflections on the related product characteristics, performances and potential applications.

This work aims to investigate the structure uniformity of mixed activated carbon (AC) nanoparticles with MWCNTs. It considers mixing different ratios of MWCNTs with nanoparticles of activated carbon resorcinol-formaldehyde aerogel (AC-RFA). The mixed samples will be characterized by various techniques to show the influences of mixing. The adsorption capacity and the adsorption of gas mixtures (i.e., CH_4 and CO_2) will be studied on MWCNTAC-RFA mixed adsorbents with variable ratios. Moreover, the influence of temperature on single-component gas adsorption equilibria will be studied. The single gas adsorption capacity and predicted binary CO_2/CH_4 adsorption equilibria and selectivity onto MWCNT/AC-RFA adsorbents will be examined. Moreover, the novelty of this work lies in addressing the possible effects of carbon–carbon structural interactions and structure uniformity on the adsorption capacity and prediction of the adsorption behavior considering both the perfect-negative (PN) and perfect-positive (PP) behaviors.

2. Materials and Methods

2.1. Materials

Multi walls carbon nanotubes (MWCNTs) with lengths of ~5 μm and purity of >90%, were supplied from Sigma-Aldrich (USA) and utilized without extra refinement. Methanol (Analar, 99.8%, Sigma-Aldrich, Germany), resorcinol (99%, Sigma-Aldrich, Germany), formaldehyde (37–41% in water, Sigma-Aldrich, Germany), Na_2CO_3 (anhydrous, ACS, 100%, Fisher, Germany), HNO_3 (70.4%, Sigma-Aldrich, Germany), ammonium hydroxide (24%, Fluke, Germany), acetone (99%, BDH, England) and acetic acid (Analar, BDH, USA) were utilized as obtained. Ultra-purified H_2O generated from the Milli-Q integral purification system (Elix®70, France) was used in all experiments. Carbon aerogels were synthesized in-house as described in Sections 2.2 and 2.3. CO_2, CH_4 and N_2 gases were supplied by the National Industrial Gas Plants (NIGP, Qatar) with high purities (> 99.999%).

2.2. Synthesis of Aerogels

Aerogels were prepared from resorcinol and formaldehyde as fundamental reactants, with sodium carbonate as a catalyst. The pH level of the reaction medium was adapted at neutral level with diluted nitric acid and ammonium hydroxide solutions. The quantities of resorcinol, sodium carbonate, formaldehyde, and water that were utilized in the synthesis of the aerogel were 12.44 g, 0.0240 g, 17.40 mL, and 32.60 mL, accordingly. The temperature was kept constant at 70 $\pm$ 1 °C. Resorcinol and Na_2CO_3 were weighed and blended with ultrapure H_2O in Erlenmeyer flasks, and then stirred until all constituents are entirely dissolved. Afterwards, formaldehyde was combined with the previously dissolved species during the stirring process. After that, the solution acidity was adapted at (pH = 7) by utilizing diluted HNO_3 and NH_4OH buffers. The resorcinol–formaldehyde mixture solution was poured into vials, sealed tightly and set in an oven at 70 $\pm$ 1 °C. In order to prevent the dehydration of the gel, and to increase their cross-linking density, a dilute (2%) acetic acid solution is poured onto the gel after its solidification. After seven days, the samples were retrieved from the oven and left to cool down to ambient temperature.

The remnant solution on top of the cured gel was decanted and disposed. The remaining solution was replaced with fresh acetone at ambient temperature by casting acetone on top of the sample surface and keeping it at ambient temperature for one day, then replacing the leftover acetone with fresh acetone everyday for three consecutive days. Following the 3rd day of solvent replacement with acetone, the drying process was conducted by supercritical CO_2 extraction with the following procedure. Firstly, the gel was put underneath pressure of 20 MPa of liquid CO_2 at a temperature of 25 °C to dissolve the acetone with the liquid CO_2. The exit valve was opened and the extractor was depressurized to 12 MPa, allowing liquid CO_2 to flow through the gel at 25 °C for times ranging from 1 to 2.5 h. Then, the temperature was elevated to reach the supercritical state at 31 °C and 7.4 MPa, and maintained at this condition for 2 h. After that, the extractor was gradually depressurized to atmospheric pressure and the dried resorcinol-formaldehyde aerogel was attained [28–31]. The supercritical drying was performed using a critical point dryer (E3100 Critical Point Dryer, Quorum Technologies—Preparation for Excellence, UK). The proposed reaction mechanism of resorcinol and formaldehyde to produce a gel is represented in Figure 1.

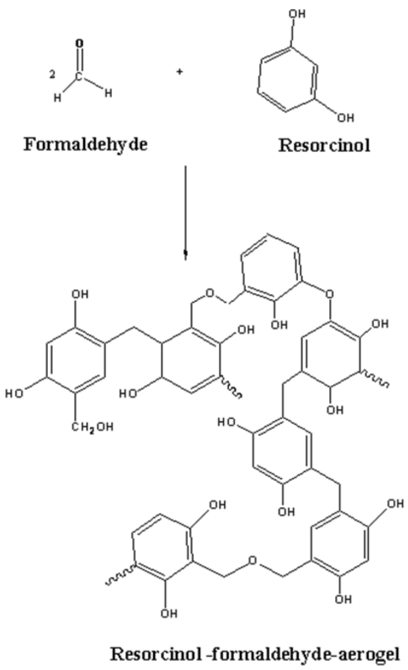

Figure 1. Suggested reaction mechanism of resorcinol-formaldehyde gel.

2.3. Preparation of Carbonized and Activated Carbon Aerogels

The dried resorcinol formaldehyde aerogels (RFA) was set in a ceramic boat in a programmable electrically-heated tube oven (Nabertherm GmbH, Germany), with flowing nitrogen gas (100 cm^3/min). The oven was initially kept at ambient temperature for 30 min to make sure that the air surrounding the samples was flushed out completely with the nitrogen gas. Next, the oven was heated to 500 °C with ramp of 10 °C/min, kept at 500 °C for 3 h, and then left to reach the ambient temperature spontaneously whilst passing nitrogen gas flow.

The resultant RF carbon aerogel was then activated in the same oven (after cleaning it thoroughly from previous process residues) with passing a CO_2 gas flow (150 cm^3/min) in place of nitrogen gas flow, heating the sample once more with a ramp of 10 °C/min to 700 °C, keeping the sample at 700 °C for 1 h, and then letting the sample to reach the ambient temperature spontaneously whilst passing CO_2 gas [32]. The produced sample is considered to be an activated carbon aerogel (AC-RFA). Figure 2 illustrates a schematic diagram of the carbonization and activation processes of RFA sample.

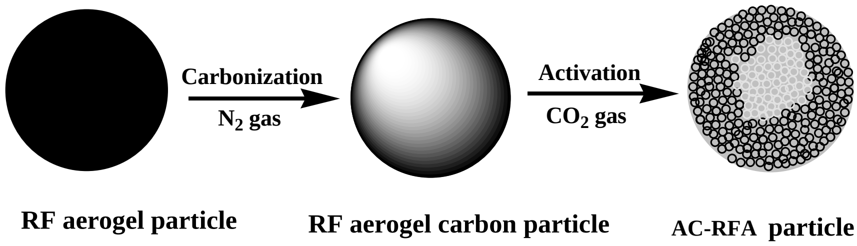

Figure 2. The carbonization and activation processes of RF aerogel sample.

2.4. Mixing of MWCNTs and AC-RFAs

The MWCNTs and AC-RFAs were mixed in variable mass proportions in refluxing with methanol during stirring for 24 h at 50 °C. These samples are then dried at 110 °C for 3 days to be ready for adsorption. The samples denoted as S100, S60, S50, S40 and S0, respectively, refer to mass percentages of 100% MWCNTs (0% AC-RFAs), 60% MWCNTs (40% AC-RFAs), 50% MWCNTs (50% AC-RFAs), 40% MWCNTs (60% AC-RFAs) and 0%MWCNTs (100% AC-RFAs), respectively. It is noteworthy to mention that investigating the effects of mixing carbon–carbon nanostructures is a novel issue and may affect its related properties and applications.

2.5. Characterizations

The surface area and porosity of AC-RFA and MWCNTs samples were examined via the adsorption/desorption isotherms of nitrogen at −196 °C by a Micromeritics ASAP2420® surface area and porosity analyzer. In advance of each analysis, the specimens were degassed in-situ for 24 h at 150 °C under high vacuum (1×10^{-4} Pa). The pore properties of samples were determined from the adsorbed volume of N_2 at −196 °C and the relative pressure (P/P_0) of 0.99 (99% of the saturation pressure).

The FT-Raman spectra were collected by a Bruker FT-Raman spectrometer of type RFS 100/S that is attached to a Bruker-IFS 66/S spectrometer. The morphology of MWCNT/AC-RFA mixed specimens was observed using an FEI Nova™ nanoscanning electron microscope 450 (Nova NanoSEM). A transmission electron microscope (TEM) of Talos L120C and of FEI Tecnai G2 F20 FE-TEM, available at Qatar Environment and Energy Research Institute (QEERI), were utilized to investigate the samples. Thermogravimetric analyses (PerkinElmer Pyris 6 TGA) were proceeded under nitrogen gas flow with a ramp 10 °C/min from ambient temperature to 800 °C (see Figure S1 in Supplementary Materials).

Adsorption/desorption isotherm measurements of CO_2 and CH_4 gases were carried out by a Rubotherm-Hygra magnetic suspension microbalance with a microgram resolution [22]. Prior to the adsorption measurement process on each sample, a buoyancy measurement using helium gas was conducted at 40 °C to assess the skeleton mass and volume, and hence the skeleton density, of each sample [22]. Furthermore, before conducting every adsorption isotherm, the samples were degassed in-situ at 120 °C for 24 h (see Figure S2 in Supplementary Materials). The adsorption calculations proceed afterwards as reported elsewhere [22,24].

The elemental analysis of MWCNT/AC-RFA mixed samples were carried out using a CHNS/O analyzer (2400, Series II, Perkin Elmer). X-ray diffraction (XRD) measurements were also conducted by utilizing a Miniflex II Benchtop XRD analyzer, manufactured by Rigaku Corporation Japan. The 2θ scan data were collected over the range of 5° to 90°. X-ray photoelectron spectroscopy (XPS) was achieved utilizing a Thermo Scientific K-alpha photoelectron spectrometer using monochromatic $Al_{k\alpha}$ radiation.

3. Theory

Adsorption equilibrium data are among the basic cornerstones for simulating and optimizing adsorption systems. Numerous adsorption models exist to explain and describe these equilibrium data and their consequent physical properties. Some of the adsorption model parameters can indicate some of the adsorbent surface features, such as its adsorption affinity and energetic homogeneity/heterogeneity towards the adsorbed gas molecules.

3.1. Equilibrium Adsorption Isotherms

The forecasting of unary and binary adsorption equilibria relies on the precision of single component adsorption data and their description with a reliable adsorption isotherm model. Adsorption equilibrium data of the binary gas system (CO_2 and CH_4) is forecasted in this work from single component (unary) adsorption isotherm fitting parameters by applying the extended dual-site Langmuir (DSL) isotherm model.

The unary (single- constituent) DSL model [30] describes the adsorption of constituent i onto a nonhomogeneous surface that consists of two homogeneous, but energetically distinct, sites. Supposing that the adsorbent-adsorbate free energy onto each site is fixed, the adsorbed quantity of constituent i is determined from Equation (1)

$$n_i = \left(\frac{n^s_{1,i} b_{1,i} P}{1 + b_{1,i} P} \right)_{\text{site 1}} + \left(\frac{n^s_{2,i} b_{2,i} P}{1 + b_{2,i} P} \right)_{\text{site 2}} \tag{1}$$

where $n^s_{1,i}$ and $b_{1,i}$ correspond, respectively, to the monolayer saturation capacity limit and adsorption affinity on site 1; $n^s_{2,i}$ and $b_{2,i}$ are, correspondingly, the monolayer saturation limit and adsorption affinity on site 2, and P is pressure. The hypotheses of the traditional Langmuir model are considered valid to each site, and the two sites are assumed not to interact with each other [33]. In this formulation, the monolayer saturation limit for every constituent on each site is let to be dissimilar. The affinity parameter for the adsorption of component i is obtained from Equation (2)

$$b_{j,i} = b_{j,i_0} \exp\left(\frac{E_{j,i}}{RT} \right) \tag{2}$$

where j refers to the free-energy level (site 1 or site 2), $E_{j,i}$ is the adsorption energy of constituent i on site j, $b_{j,io}$ is the pre-exponential factor (or adsorption affinity of constituent i on site j at infinite temperature, T) and R is the universal gas constant. The corresponding Henry's law constant can be estimated from Equation (3) as

$$H_i = \lim_{P \to 0} \frac{n_i}{P} = \left(n^s_{1,i} b_{1,i} P \right)_{\text{site 1}} + \left(n^s_{2,i} b_{2,i} P \right)_{\text{site 2}} \tag{3}$$

In this formulation, j = 1 always refers to the adsorption site with a higher free energy level, and j = 2 always refers to the adsorption site with a lower free energy level. For unary gas adsorption, this causes the free energy of site 1 always superior than that of site 2.

On the other hand, for binary gas adsorption, the two free energies can be attributed to either site 1 or site 2.

For the extended DSL model, thermodynamic consistency necessitates the overall saturation capacity ($n^s_{1,i} + n^s_{2,i}$) to be similar for all the constituents [34]. Equivalently, the amounts $n^s_{1,i}$ and $n^s_{2,i}$ in extended DSL would not depend on the constituent [35]. Unary constituent adsorption equilibrium data for each of CO_2 and CH_4 gases were fitted to the DSL isotherm model (Equations (1) and (2)) by the method of the least sum of squared errors (*LSSE*) as shown in Equation (4). Moreover, the percentage average relative error (*ARE*, %) between the measured and correlated quantities adsorbed is assessed from Equation (5).

$$LSSE = minimum\left\{\sum_{i}^{N_P}\left(n_{cal} - n_{exp}\right)^2_i\right\} \tag{4}$$

$$ARE(\%) = \frac{100\%}{N_p}\sum_{i}^{N_P}\left|\frac{n_{cal} - n_{exp}}{n_{exp}}\right|_i \tag{5}$$

where i refers to the data point number, N_P refers to the total number of data points for every constituent, and the subscripts "*exp*" and "*cal*" symbolize, correspondingly, the experimental and correlated amounts. It is important to mention that the theoretical background of binary equilibrium adsorption isotherm is illustrated in the Supplementary Materials.

3.2. Selectivity

Further to the forecasting of equilibrium adsorption capacity by extended DSL model, the selectivity of adsorbing constituent A over constituent ($S_{A,B}$) in the gas mixture of A and B can be assessed by [36].

$$S_{(A,B)} = \frac{\left(\frac{x_A}{y_A}\right)}{\left(\frac{x_B}{y_B}\right)} \tag{6}$$

where x_A and y_A refer to the mole fractions of constituent A in the adsorbed and gas phases, correspondingly. The same can be noted about x_B and y_B. The values of x_A and x_B can be calculated from

$$x_A = \frac{n_{A,m}}{n_{A,m} + n_{B,m}};\quad x_B = \frac{n_{B,m}}{n_{A,m} + n_{B,m}} = 1 - x_A \tag{7}$$

where $n_{A,m}$ and $n_{B,m}$ are the amounts adsorbed of constituents A and B, respectively, from the binary mixture, and can be calculated from the extended DSL model as illustrated in the Supplementary Materials.

4. Results and Discussion

Figure 3 illustrates the Raman spectra of MWCNT/AC-RFA mixed samples with variable compositions. These samples (with MWCNT:AC-RFA weight ratios of 100:0, 60:40, 50:50, 40:60 and 0:100) were labeled as S100, S60, S50, S40, and S0, respectively. The spectra of carbon structures contain two main bands: the G-peak (at 1576 cm^{-1}) and D-peak (at 1314 cm^{-1}). The G-peak is attributed to the stretching mode of a well-ordered graphitic matrix, whereas the D-peak is assigned to the stretching mode of a defected structure or lattice in the graphite matrix (e.g., vacancies or substitutional heteroatoms or chemically attached heteroatoms) [37]. The quotient of the D-peak (I_D) to the G-peak (I_G) intensities in Raman spectra is a useful parameter to assess the structural ordering/disordering of carbons, comprising carbon nanostyles. A high I_D/I_G indicates to the existence of disorders within the carbon matrix, whereas a low value of I_D/I_G refers to a degree of crystalline perfection and less structure defects. The trend in Figure 4 shows that by increasing the ratio of AC-RFA into the sample, the I_D/I_G ratio value increases. The increment relates to increasing disorder and defects of carbon materials. The peak at 2623 cm^{-1} (G″-peak) for MWCNTs in Figure 3 refers to an overtone of the D-peak [38]. In further observation, it was seen that peak at 856 cm^{-1} appears for S100 and disappears for S0.

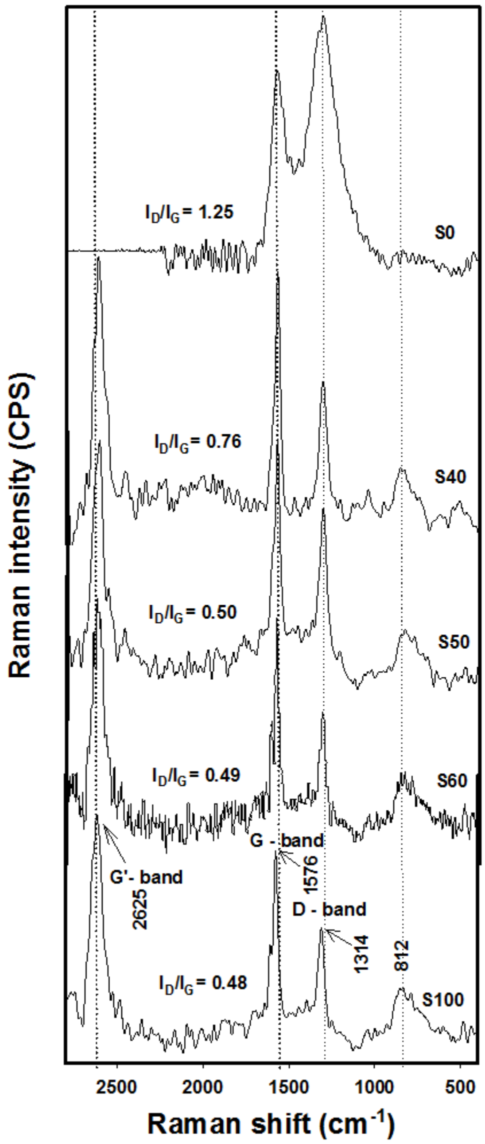

Figure 3. Raman spectra of different MWCNT/AC-RFA mixed sample compositions; namely S100, S60, S50, S40 and S0.

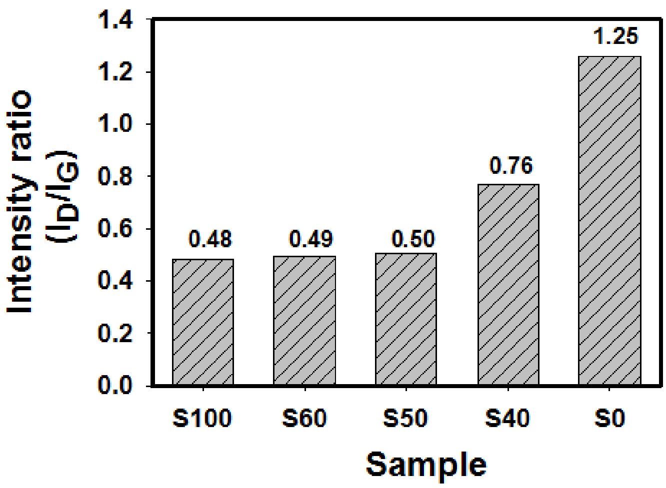

Figure 4. Effect of MWCNT/AC-RFA mixed sample compositions on the I_D/I_G intensity ratios.

Figure 5a–e shows NanoSEM photomicrographs of S100, S60, S50, S40 and S0 samples, respectively. The difference in the morphology of these samples is observed clearly as a reflection of increasing content of carbon nanospheres among the carbon nanotubes. Figure 6a–e shows TEM images of S100, S60, S50, S40 and S0 samples, respectively. The observations from these images support those deduced from NanoSEM photomicrographs. The elemental analyses of these samples were carried out using CHNS/O and XPS techniques The elemental analyses, either from EDX or XPS, indicate that as the oxygen percentage is higher, the adsorption capacity increases as listed in Table S1 (Supplementary Materials).

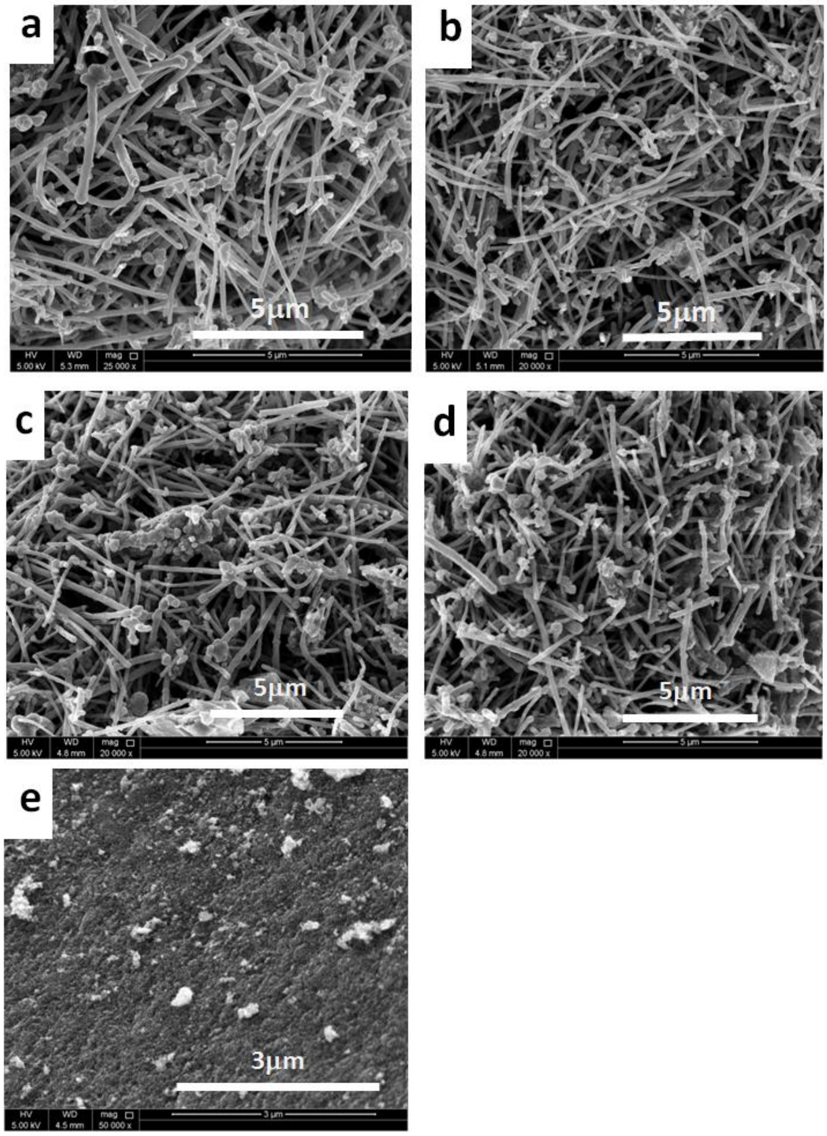

Figure 5. NanoSEM photomicrographs of different MWCNT/ AC-RFA mixed sample compositions; namely (**a**) S100, (**b**) S60, (**c**) S50, (**d**) S40 and (**e**) S0.

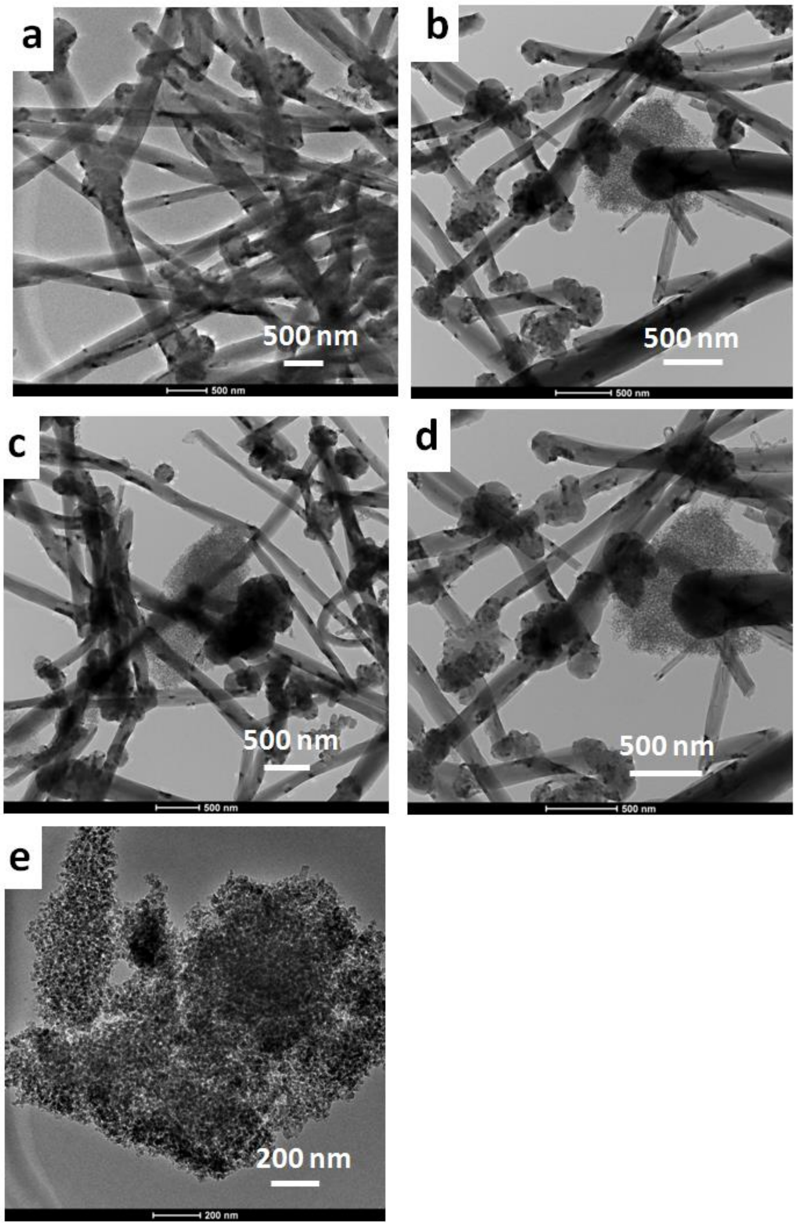

Figure 6. TEM photomicrographs of different MWCNT/AC-RFA mixed sample compositions; namely (**a**) S100, (**b**) S60, (**c**) S50, (**d**) S40 and (**e**) S0.

The nitrogen adsorption/desorption isotherms at −196 °C on S100, S60, S50, S40, and S0 are exposed in Figure 7. The isotherms of N_2 gas adsorption/desorption at −196 °C on pure MWCNTs (i.e., the sample of S100) are classified as a type-II adsorption isotherm as defined by IUPAC. This type is often encountered in adsorption by nonporous substances or in substances with macropores or unlocked cavities [39]. Furthermore, it is noticed that almost no hysteresis exists for the sample S100, whereas it appears noticeably in the samples S60, S50, S40 and S0. The nitrogen adsorption capacities onto the samples S60, S50, S40 and S0 samples are significantly higher than that onto the sample S100. This might be because the adsorption on mesoporous AC-RFA that is present in the mixed samples ensues through multilayer adsorption pursued by capillary condensation, resulting in type-IV isotherm [40,41]. Generally, hysteresis is attributed to a thermodynamic effect, a network effect (or a combination of these two effects) and capillary condensation as well [42]. It was observed that the hysteresis on pure MWCNTs is almost zero, while the hysteresis on AC-RFA is noticeable. Moreover, the porosity of AC-RFA is higher than that of MWCNTs. Consequently, the capillary condensation effect occurs more significantly in AC-RFA than MWCNTs; and the results listed in Table S2 (Supplementary Materials) support this behavior. Overall, as is reported in the literature, there are five types of hysteresis loops and their related pore shapes. Namely, Type-A is attributed to cylindrical pores; Type-B is assignable to slit pores; Types-C and -D are assignable to wedge shaped pores and Type-E is attribute to bottle neck pores [43]. The hysteresis loops in this work belong to Type-E, which indicates to bottle neck pore type.

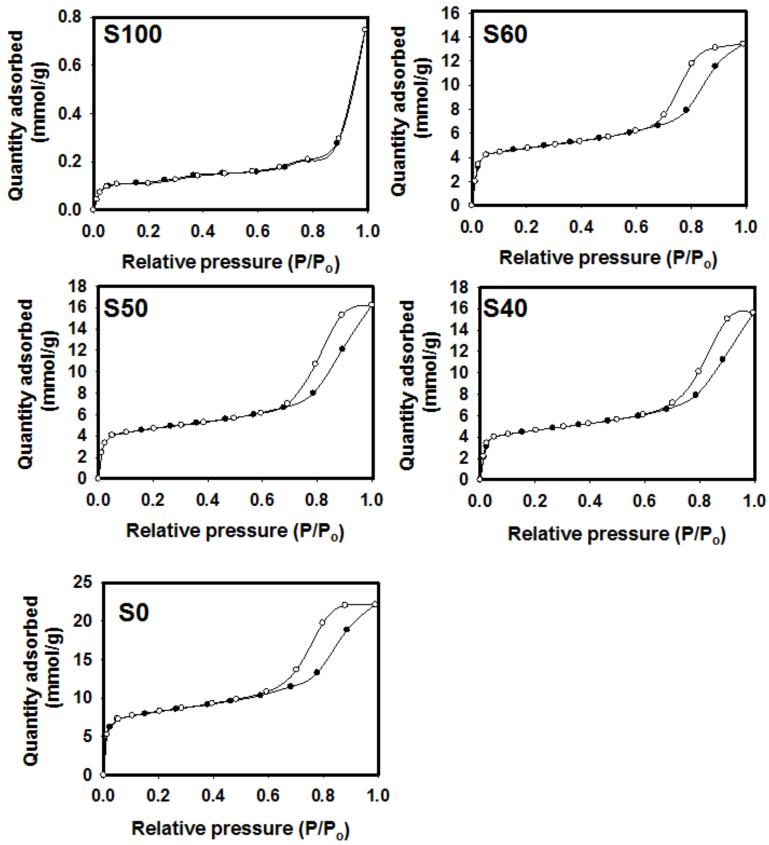

Figure 7. Isotherms of N_2 adsorption/desorption at −196 °C onto different MWCNT/AC-RFA sample compositions; namely S100, S60, S50, S40 and S0. Solid circles refer to adsorption data and empty circles refer to desorption data.

Through the results listed in Table 1, it is seen from the S60 to S0 samples that the neck of the mesopore opens at a P/P_o range between ~0.7 and 1; as shown by the observed hysteresis loops [44]. This indicates that all the samples from S60 to S0 exhibit mesoporous structures. The pore volume of samples changed from 0.026 to 0.767 cm^3/g when comparing S100 to S0, respectively; and the average pore size changed from 63.7 to 6.1 nm when comparing S100 to S0, respectively (Table 1). Moreover, BET surface area changed from 1.63 to 507 m^2/g, respectively (Table 1). This conclusion is agreement with the structural properties of the samples as listed in Table 1.

Table 1. Structural properties of different mixed MWCNT/AC-RFA compositions.

Sample ID	Density [a] (g/cm^3)	Pore Volume [b] (cm^3/g)	BET Surface Area [b] (m^2/g)	Average Pore Size [b] (nm)
S100	0.355	0.026	1.63	63.7
S50	0.373	0.525	158	14.2
S40	0.380	0.551	296	7.4
S0	0.394	0.767	507	6.1

[a] Density values were calculated from buoyancy experiments in helium. [b] These values are determined by using Micromeritics 2420 Surface Area and Porosity Analyzer.

Figure 8 exposes the XRD patterns of different MWCNT/AC-RFA mixed sample compositions; namely S100, S60, S50, S40 and S0. It is noted that the peaks at 2θ of 26.1°, 42° and 54° are assigned, respectively, to the (002), (100) and (004) planes of the hexagonal graphite structure of the MWCNTs [37,45]. It was observed that the fingerprint band of MWCNTs (2θ = 26.1°) exposed a diminuendo trend when increasing amount of AC-RFA into the mixed sample composition. Furthermore, other two small peaks at 21.4° and 54° were noticed in the samples ranging from S100 to S40 and disappeared in S0. It could be said through outcome results that the sharp peak at 26.1° and broad peaks at 21.4° refer, respectively, to the relative crystallinity and relative amorpohicity regions into the samples. The characteristic peak of MWCNTs at 26.1° diminished gradually when increasing the quantity of AC-RFA into the composition. Figure 9a is a summary of FWHM of XRD peaks at 2θ values of 26.1° and 21.4°, which indicate to the relative crystalline section of MWCNTs and relative amorphous section of AC-RFA, correspondingly. It was observed that the FWHM of the band at 26.1° has a diminuendo trend, whereas that at 21.4° has a crescendo behavior with the increase in the AC-RFA ratio. Figure 9b represents the influence of the hybrid MWCNT/AC-RFA mixed sample composition on the XRD FWHM ratio ($I_{26.1°}/I_{21.4°}$). The ratio of XRD peaks ($I_{26.1°}/I_{21.4°}$) increases with the increasing MWCNT content; thereby increasing the relative crystallinity and reducing the relative amorphicity into the matrix of the product. Figure 9c exhibits the impact of sample composition on FWHM of XRD peaks at 2θ of 42° and 54°, which evidently show that no significant influence on the intensity of these peaks is noticed when adding AC-RFA to MWCNTs, whereas the pure AC-RFA (i.e., the sample of S0) has no such peaks.

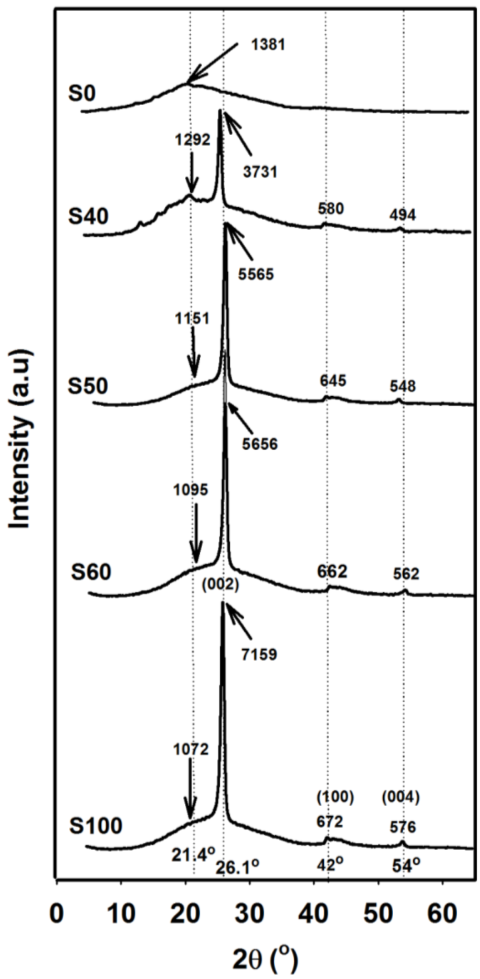

Figure 8. XRD patterns of different MWCNT/AC-RFA compositions; namely samples of S100, S60, S50, S40 and S0. The values on pattern peaks indicate to their corresponding intensities.

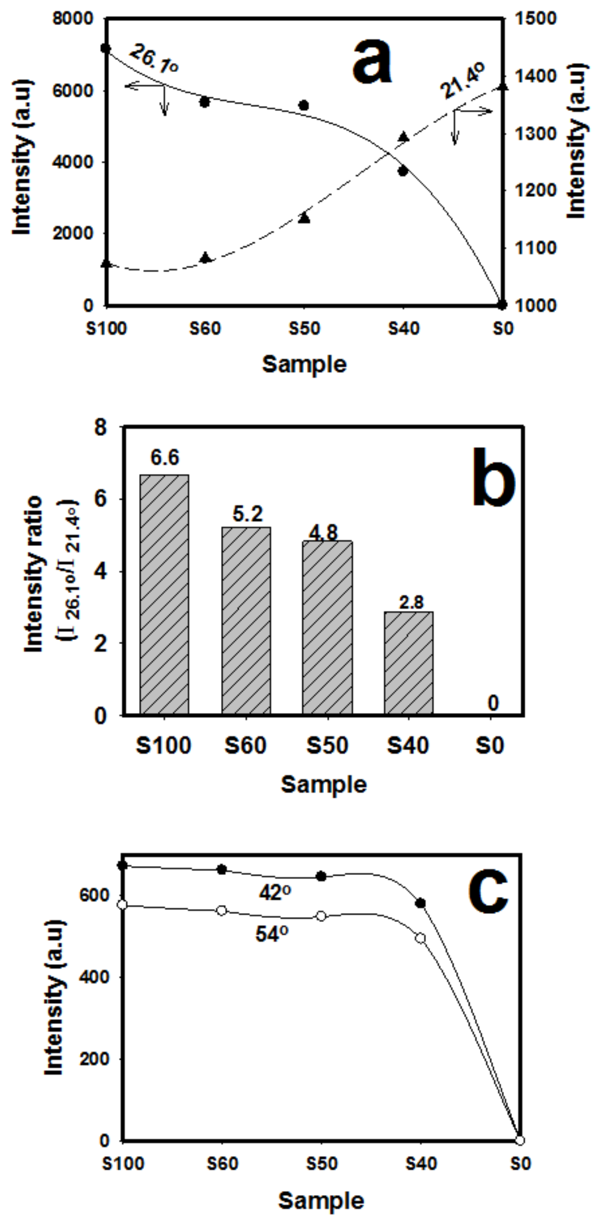

Figure 9. Impact of hybrid MWCNT/AC-RFA sample composition on the XRD (**a**) intensities of the peaks at 2θ of 26.1° and 21.4° (**b**) intensity ratio (I26.1°/I21.4°) and (**c**) intensities at 2θ of 42° and 54°.

Figure 10 shows the isotherms of CO_2 and CH_4 gases adsorption/desorption isotherms at 40 °C versus pressure onto hybrid MWCNT/AC-RFA adsorbents with various compositions, namely S100, S60, S50, S40, and S0. It is observed that the adsorption capacities of CO_2 and CH_4 increase by increasing the ratio of AC-RFA into the hybrid MWCNT/AC-RFA adsorbent, which can be attributed to the increased surface area (see Table 1), and enhance the interactions between the adsorbing surface and gas molecules. The sequential order of hybrid MWCNT/AC-RFA samples towards either CO_2 or CH_4 is as S0 > S40 > S50 > S60 > S100. Furthermore, the adsorption affinity of all samples towards CO_2 is higher than that towards CH_4. All isotherms described in Figure 10 are classified as Type-I according to IUPAC [46]. However, the sample S100 exposes an almost linear adsorption isotherm for both CH_4 and CO_2.

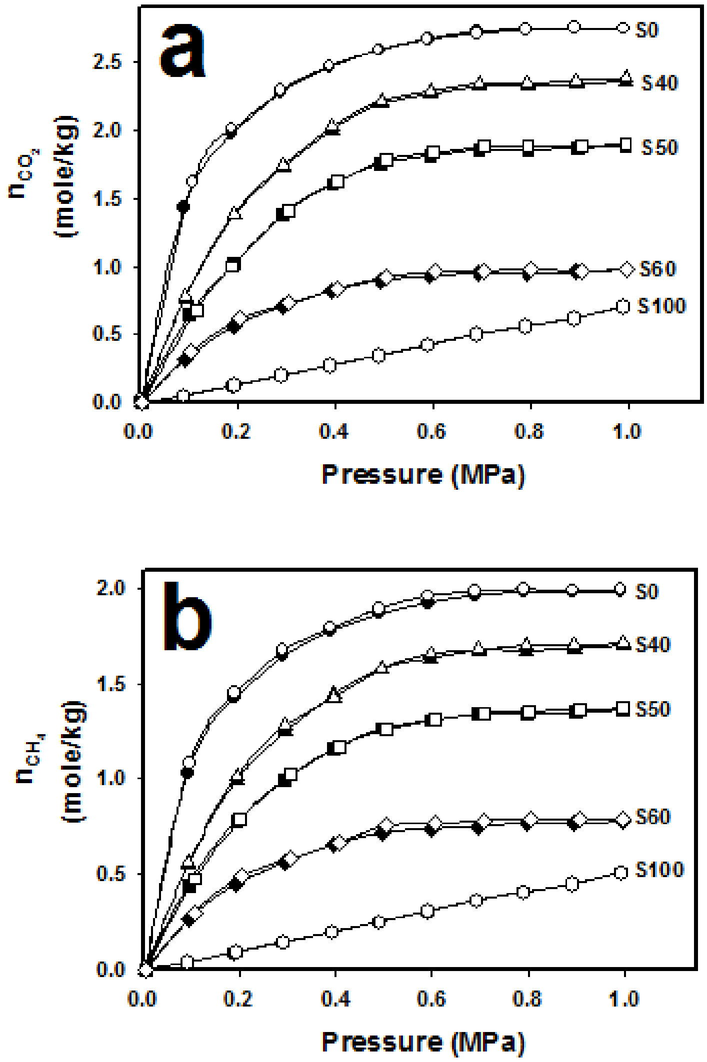

Figure 10. Adsorption/desorption isotherms of (**a**) CO_2 and (**b**) CH_4 on different hybrid MWCNT/AC-RFA sample compositions; namely, S100, S60, S50, S40 and S0 at 40 °C. Solid and empty symbols indicate, correspondingly, the experimental adsorption and desorption data.

From Raman results, the trend of uniformity deduced from I_D/I_G ratio leads to affecting the adsorption capacity; which is also supported by pore and area structure data listed in Table 1. Overall, the higher ratio of I_D/I_G indicates more defects/disorders into the matrix is, which results in higher adsorption capacities. On other words, the by increasing the amount of AC-RFA into the adsorbent matrix, the adsorption capacity of adsorbent increases.

Further, the XRD profiles indicate that as more RFA-AC is added to MWCNTs, a higher adsorption capacity is attained due to the increasing amorphicity of the structure. It is important to mention that the crystallinity of MWCNTs is higher than that of RFA-AC. The elemental analysis, either from EDX or XPS, indicates that as the oxygen percentage is higher, the adsorption capacity increases as shown in Table S1 (Supplementary Materials). In addition to the former results based on Raman and XRD patterns discussed previously, it could be said that by increasing the AC-RFA, the increasing non-uniformity of the adsorbent corresponds to higher adsorption capacities towards gas molecules. Therefore, the adsorption capacity of adsorbents is enhanced by increasing the non-uniformity order into the structure of sample utilized, which also corresponds to a higher surface area and pore volumes as presented in Table 1. Therefore, structural characteristics such crystallinity, composition, and orders/disorders have a significant impact on the adsorption behavior of CH_4 and CO_2 gases.

Figure 11a,b exposes the adsorption/desorption isotherms of CO_2 and CH_4 gases onto the sample S50 at 20, 40, and 60 °C. The adsorption capability of S50 towards each of CO_2 and CH_4 reduces noticeably when increasing temperature. The symbols and lines represent experimental points and DSL correlations, respectively. It was observed from Figure 11 that the experimental points are well fitted by the DSL model for both CO_2 and CH_4 gases; covering the whole range of pressure and temperature scales as well. Therefore, the DSL model is deemed to be an excellent presentation of experimental data over the whole ranges of pressure and temperature. Trials showed that two homogenous sites (i.e., J = 2) are adequate to define the adsorption of CO_2 or CH_4 gases via the DSL model. The optimum fitting parameters, along with the corresponding *LSSE* and *ARE*(%) values deduced from cumulative adsorption data of each component over the entire range temperature, are listed in Table S3 (Supplementary Materials).

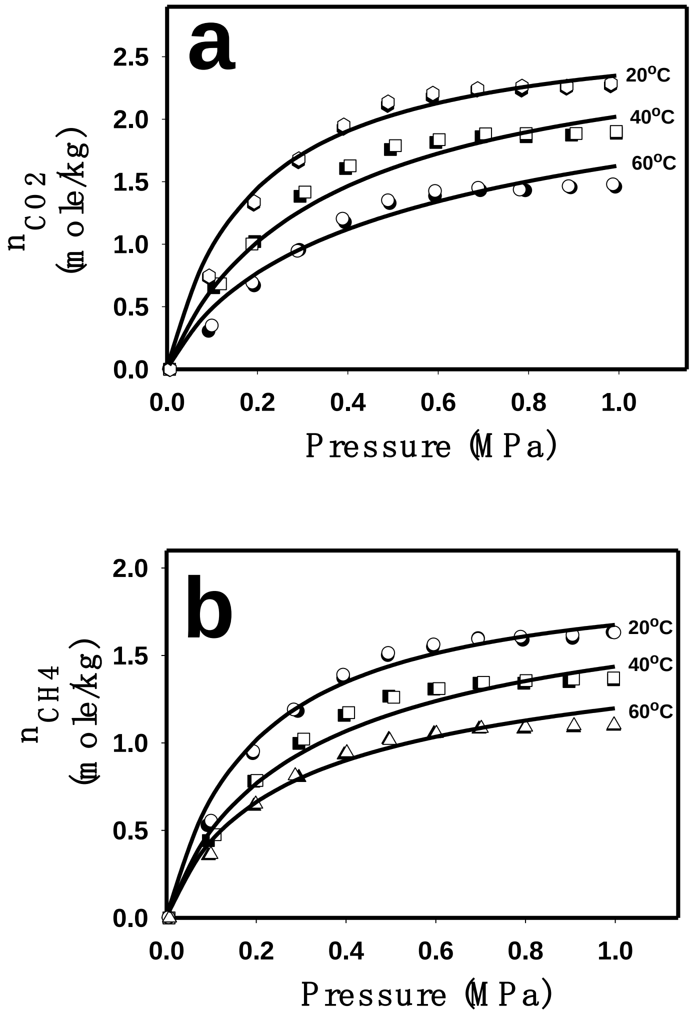

Figure 11. Experimental (symbols) and DSL fitting (lines) adsorption equilibrium points of (**a**) CO_2 and (**b**) CH_4 gases onto S50 at various temperatures. Solid and empty symbols refer, respectively, to adsorption and desorption points.

The unary constituent adsorption of CO_2 and CH_4 gases onto the sample S50 were fitted well by the DSL isotherm model, as described in the previous section. The adsorption equilibria of dual mixtures of CO_2 and CH_4 gases were forecasted utilizing both the PP (Equations (S2) and (S3)) and PN (Equations (S4) and (S5)) behaviors of the DSL model with merely the unary gas adsorption regression parameters listed in Table S3 (Supplementary Materials). No binary data were needed to forecast the dual adsorption equilibrium data. The predicted effects of the mole fraction of CO_2 in the adsorbed phase (x_{CO_2}) on the gas-phase mole fraction of CO_2 (y_{CO_2}) and selectivity of adsorbing CO_2 relative to CH_4 (S_{CO_2,CH_4}) are illustrated in Figure 12.

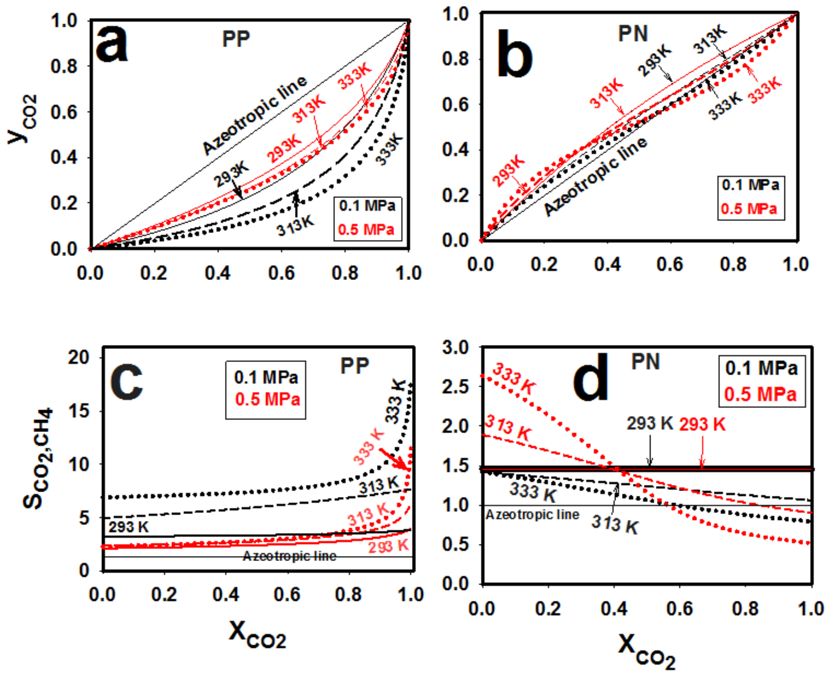

Figure 12. Predicted binary adsorption gas mole fractions (**a**,**b**) and selectivity of adsorbing CO_2 from CH_4 (**c**,**d**) onto the sample S50 at 0.1 and 0.5 MPa (black and red lines, correspondingly). Subfigures a and c represent PP behavior and the subfigures b and d represent PN behavior.

Figure 12a,b show the predicted relationships between x_{CO_2} and y_{CO_2} for the PP and PN behaviors, respectively, at various temperatures, and at both minimal and high pressures (0.1 MPa and 0.5 MPa, respectively). It is noticed that y_{CO_2} increases with increasing x_{CO_2}. However, Figure 12a exposes that the PP behavior always predicts higher x_{CO_2} than y_{CO_2} at all temperatures. Therefore, the PP predicts no azeotropic behavior between CO_2 and CH_4 gases at the full scale of temperature. At a high pressure (0.5 MPa), y_{CO_2} increases very slightly with increasing temperature. At any x_{CO_2}, the value of y_{CO_2} at 0.5 MPa is always higher than that at 0.1 MPa. It is observed from Figure 12b that at a low temperature (293 K), the PN behavior predicts no azeotropic conditions in the full range of x_{CO_2} with coinciding curves at both low and high pressures (0.1 and 0.5 MPa, respectively). Furthermore, at medium temperature (313 K), an azeotropic behavior is predicted at x_{CO_2} of ~ 0.85 only at high pressure. Furthermore, at an elevated temperature (333 K), azeotropic behaviors are predicted at x_{CO_2} of ~0.55 in states of both minimal and elevated pressures. At any x_{CO_2}, the value of y_{CO_2} corresponding to the PN behavior (Figure 12b) is higher than that corresponding to the PP behavior (Figure 12a).

Figure 12c,d illustrate the predicted relationships between x_{CO_2} and S_{CO_2,CH_4} for the PP and PN behaviors, respectively, at different temperatures and at both low and high pressures (0.1 MPa and 0.5 MPa, respectively). It was observed from Figure 12c that the PP behavior predicts that, at a low temperature (293 K), S_{CO_2,CH_4} is constant at 3.25 and 2.33 in the cases of a low or a high pressure (0.1 and 0.5 MPa), respectively. Nonetheless, at higher temperatures (313 and 333 K), S_{CO_2,CH_4} increases when increasing x_{CO_2}, especially at 333 K when $x_{CO_2} > 0.8$. Moreover, S_{CO_2,CH_4} was higher at minimal pressure (0.1 MPa) than that at elevated pressure (0.5 MPa), and no azeotropes were predicted at both pressures. On the other hand, it can be seen from Figure 12d that the S_{CO_2,CH_4} predicted by the PN behavior at low temperature was constant at 1.5, regardless of x_{CO_2} or pressure. However, at higher temperatures (313 and 333 K), it decreases when increasing x_{CO_2} at both minimal and elevated pressures (0.1 and 0.5 MPa). At a moderate temperature (313 K), the value of

S_{CO_2,CH_4} predicted at elevated pressure (0.5 MPa) is lower than that at minimal pressure (0.1 MPa) when $x_{CO_2} > \sim 0.65$. Furthermore, at a high temperature (333 K), the value of S_{CO_2,CH_4} at elevated pressure (0.5 MPa) is lower than that at minimal pressure (0.1 MPa) when $x_{CO_2} > \sim 0.56$. The azeotropic behavior appeared at x_{CO_2} of ~0.85 at moderate temperature (313 K) and high P (0.5 MPa), and at x_{CO_2} of ~ 0.55 at high temperature (333 K) for both pressures. The selectivity in both behaviors (i.e., PP and PN) is affected significantly by the structure adsorbents, adsorption capacity and temperature. Increasing surface area and pore volume (as presented in Table 1) enhance the adsorption capacity. This is due to an increase in the AC-RFA content in the mixed adsorbent, which makes its structure more amorphous. Furthermore, it is reported in the literature that an incompetence of MWCNTs persists for the adsorption or selectivity of gases [47–49], while activated carbons generally expose good adsorption capacities and selectivities of gases [50–52]. Therefore, adding AC-RFA to MWCNTs enhances the adsorption capacity and selectivity based on adsorption isotherms as preliminary data. It is to be noted that the recent data of only S50 are not enough to discuss the full range of MWCNTs to AC-RFA ratios and their effects on selectivity, specifically.

Figure 13a–d illustrates the predicted relationship between pressure and adsorption performance (i.e., Figure 13a,c exposing n_{CO_2} and n_{CH_4} and Figure 13b,d exposing S_{CO_2,CH_4}) for an equimolar gas mixture of CO_2 and CH_4 at different temperatures for the (a, b) PP and (c,d) PN behaviors. Figure 13a shows that both n_{CO_2} and n_{CH_4} predicted by the PP behavior increase by either decreasing the temperature or by increasing the pressure. Moreover, it is observed from Figure 13b that the S_{CO_2,CH_4} predicted by the PP behavior increases by increasing the exposed pressure at 313 and 333 K, but remains constant at 293 K. The value of S_{CO_2,CH_4} increases when decreasing temperature, especially at low to moderate pressures. Figure 13c,d exposes the PN behavior relationship between n_{CO_2} and pressure for an equimolar feed gas mixture of CO_2 and CH_4 at 293, 313 and 333 K. It is noticed that the n_{CO_2} and n_{CH_4} both increase with increasing pressure at all temperatures. The value of n_{CO_2} increases by decreasing temperature, whereas that of n_{CH_4} is almost independent of temperature. If the values of n_{CO_2} of Figure 13a,b are compared to those of Figure 13c,d, it can be seen that the PP and PN behaviors are around the same average value. The values of S_{CO_2,CH_4} at different temperatures increase very slightly by increasing the pressure at 313 and 333 K, and remain constant at 293 K. Further, S_{CO_2,CH_4} decreases with an increasing temperature. The impact of temperature and pressure on n_{CH_4} is very small and almost insignificant in the case of PN behavior, while it is observable in the case of PP behavior.

Table 2 exposes a comparison of adsorption capacities of CO_2 and CH_4 on AC-RFA (this work) against some data reported in the literature. It can be observed that AC-RFA has a higher adsorption capacity than other adsorbents such as AC-coconut-shells, shale, AC-waste tea, etc. The adsorption capacity of AC-RFA towards CO_2 is lower than those on AC-commercial and AC-CCVD. Moreover, the adsorption capacity of AC-RFA towards CH_4 is lower than that of AC-hard coal, AC-CCVD, AC-xerogels, AC-Maxsorb II and AC-Clay-rich shale. Overall, it can be said that AC-RFA has a good adsorption capacity towards both CO_2 and CH_4 gases.

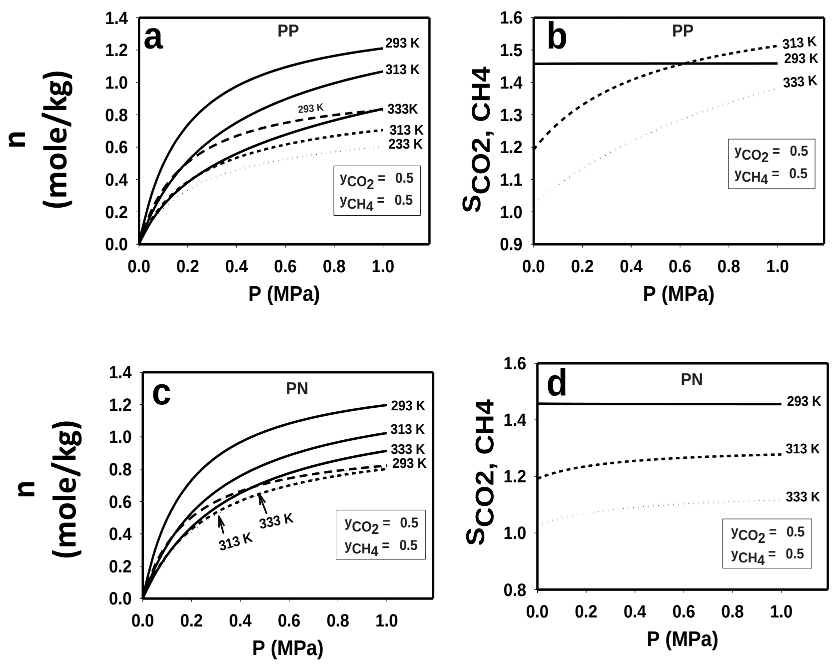

Figure 13. Binary amounts adsorbed (**a**,**c**) and selectivity (**b**,**d**) for an equimolar gas mixture of CO_2 and CH_4 onto the sample S50 predicted with the (**a**,**b**) PP and (**c**,**d**) PN behaviors. The amounts adsorbed of CO_2 and CH_4 are presented by solid and dashed lines, respectively.

Table 2. A comparative study of recent work with some literature work. The reported values are at ~1 MPa and room temperature.

Sample	Gas	Adsorption Capacity (mole/kg)	Reference
AC-RFA	CO_2	~2.79	This study
	CH_4	~2	This study
Shale	CO_2	0.172	[53]
	CH_4	0.136	
AC-coconut-shells	CO_2	2.55	[54]
AC- fibers	CO_2	0.7	[55]
	CH_4	0.3	
AC-Wood pellets	CO_2	2.32	[56]
AC-Waste tea	CO_2	1.98	[57]
AC-Modified Waste	CO_2	2.47	
AC-lotus stems	CO_2	3.85	[58]
AC-commercial	CO_2	6.123	[59]
AC- hard coal	CH_4	7.43	[60]
AC-CCVD	CH_4	4.01	[61]
	CO_2	6.41	
AC-indigenous shells	CH_4	0.48	[62]
AC-xerogels	CO_2	1.5–3	[63]
	CH_4	4.5–5	
AC-Maxsorb II	CH_4	0.25–8.1875	[64]
AC-Clay-rich shale	CH_4	3.85	[65]

5. Conclusions

Resorcinol-formaldehyde aerogels and their subsequent activated carbons (AC-RFA) were prepared. Multiwall carbon nanotubes (MWCNTs) and AC-RFA were mixed together with various ratios. Samples were characterized by various devices. Adsorption/desorption isotherms of pure CO_2 and CH_4 gases on each sample were studied. The impact of temperature on the adsorption/desorption isotherms of gases was conducted on the sample of medium composition (S50). One of key findings of this study is that the carbonaceous adsorbent structure uniformity and its order have a significant influence on pore structure, adsorption capacity and adsorption selectivity towards gases. Moreover, the highest adsorption capacity for either CO_2 or CH_4 gases was for the sample that did not contain any MWCNTs; whereas adding AC-RFA to MWCNTs enhances their adsorption capacity. Furthermore, it can be deduced that the adsorption capacity of MWCNTs towards gases is relatively very low compared to AC-RFA.

The pure-component dual site Langmuir (DSL) isotherm model was applied to correlate the adsorption data onto S50 over the entire scale of pressure at various temperatures. Moreover, the extended DSL model was utilized for predicting the adsorption equilibrium of the binary gas mixture of CO_2 and CH_4 with perfect-positive (PP) and perfect-negative (PN) behaviors at various temperatures. The selectivity of adsorbing CO_2 from CO_2/CH_4 gas mixtures was also investigated.

This study also indicated some key findings, such as the point that the adsorption of gases can follow either of the PP or PN behaviors; while the adsorption capacities are not significantly affected by the followed adsorption behavior (i.e., PP or PN behavior). Nonetheless, the adsorption selectivity is affected significantly, if the adsorption trend follows either of the PP or PN behaviors.

In the future, it is anticipated that further investigations will be carried out to improve the selectivity and adsorption capacity as well by studying different forms of carbon–carbon hybrid nanostructures. Different carbons such as SWCNTs, graphene oxides, reduced graphene oxides, graphite, etc., can be studied to evaluate their hybrid nanostructures. Furthermore, the interactions between these different carbon nanostructures shall be examined to track their mechanisms and potential applications for gas adsorption or otherwise in detail.

Supplementary Materials: Supplementary materials can be found at https://www.mdpi.com/2076-3417/11/1/265/s1.

Author Contributions: Conceptualization, A.A.-F. and S.A.A.-M.; methodology, A.A.-F. and S.A.A.-M.; validation, A.A.-F. and S.A.A.-M.; formal analysis, A.A.-F.; investigation, A.A.-F.; resources, S.A.A.-M.; data curation, A.A.-F.; writing—original draft preparation, A.A.-F.; writing—review and editing, S.A.A.-M.; visualization, A.A.-F. and S.A.A.-M.; supervision, S.A.A.-M.; project administration, S.A.A.-M.; funding acquisition, S.A.A.-M. All authors have read and agreed to the published version of the manuscript.

Funding: This research was funded by Qatar National Research Fund (QNRF), Qatar; grant number NPRP 08-014-2-003.

Acknowledgments: This publication was made possible by the NPRP award (NPRP 08-014-2-003) from the Qatar National Research Fund (a member of Qatar Foundation). Statements made herein are the sole responsibility of the authors. Technical support from the Department of Chemical Engineering, Central Laboratory Unit (CLU) and Gas Processing Centre (GPC) at Qatar University is also acknowledged. Further, the publication of this article was funded by the Qatar National Library.

Conflicts of Interest: The authors declare no conflict of interest.

References

1. Littlefield, J.A.; Marriott, J.; Schivley, G.A.; Skone, T.J. Synthesis of recent ground-level methane emission measurements from the U.S. natural gas supply chain. *J. Clean. Prod.* **2018**, *148*, 118–126. [CrossRef]
2. Olajossy, A. Some parameters of coal methane system that cause very slow release of methane from virgin coal beds (CBM). *Int. J. Min. Sci. Technol.* **2017**, *27*, 321–326. [CrossRef]
3. Rahman, K.A.; Ramesh, A. Effect of reducing the methane concentration on the combustion and performance of a biogas diesel predominantly premixed charge compression ignition engine. *Fuel* **2017**, *206*, 117–132. [CrossRef]
4. Ahoughalandari, B.; Cabral, A.R. Landfill gas distribution at the base of passive methane oxidation biosystems: Transient state analysis of several configurations. *Waste Manag.* **2017**, *69*, 298–314. [CrossRef] [PubMed]
5. Rios, R.B.; Stragliotto, F.M.; Peixoto, H.R.; Torres, A.E.B.; Bastos-Neto, M.; Azevedo, D.C.S.; Cavalcante, C.L., Jr. Studies on the adsorption behavior of CO_2-CH_4 mixtures using activated carbon. *Braz. J. Chem. Eng.* **2013**, *30*, 939–951. [CrossRef]
6. Cavenati, S.; Grande, C.A.; Alírio, E.R. Adsorption equilibrium of methane, carbon dioxide, and nitrogen on zeolite 13X at high pressures. *J. Chem. Eng. Data* **2004**, *49*, 1095–1101. [CrossRef]

7. Gholipour, M.M.F.G. Gas adsorption separation of CO_2/CH_4 system using zeolite 5A. *Microporous Mesoporous Mater.* **2014**, *200*, 1–10.
8. Gholipour, F.; Mofarahi, M. Adsorption equilibrium of methane and carbon dioxide on zeolite 13X: Experimental and thermodynamic modeling. *J. Supercrit. Fluids* **2016**, *111*, 47–54. [CrossRef]
9. Xu, X.; Song, C.; Miller, B.G.; Scaroni, A.W. Adsorption separation of carbon dioxide from flds gas of natural gas- fired boiler by a novel nanoporous "molecular basket" adsorbent. *Fuel Process Technol.* **2005**, *86*, 1457–1472. [CrossRef]
10. Iarikov, D.D.; Hacarlioglu, P.; Oyama, S.T. Supported room temperature ionic liquid membranes for CO_2/CH_4 separation. *Chem. Eng. J.* **2011**, *166*, 401–406. [CrossRef]
11. Ghoufi, A.; Gaberova, L.; Rouquerol, J.; Vincent, D.; Llewllyn, P.; Maurin, G. Adsorption of CO_2, CH_4 and their binary mixture in faujasite NaY: A combination of molecular simulations with gravimetry–manometry and microcalorimetry measurements. *Microporous Mesoporous Mater.* **2009**, *119*, 117–128. [CrossRef]
12. Nazari, L.; Sarathy, S.; Santoro, D.; Ho, D.; Ray, M.B.; Xu, C.C. *Direct Thermochemical Liquefaction for Energy Applications*; Elsevier: Amsterdam, The Netherlands, 2018; pp. 67–100.
13. Bae, Y.; Mulfort, K.L.; Frost, H.; Ryan, P.; Punnathanam, S.; Broadbelt, L.J.; Hupp, J.T.; Snurr, R.Q. Separation of CO_2 from CH_4 using mixed-Ligand metal-organic frameworks. *Langmuir* **2008**, *24*, 8592–8598. [CrossRef]
14. Zhang, X.-Q.; Li, W.-C.; Lu, A.-H. Designed porous carbon materials for efficient CO_2 adsorption and separation. *New Carbon Mater.* **2015**, *30*, 481–501. [CrossRef]
15. Wiśniewski, M.; Koter, S.; Terzyk, A.P.; Włoch, J.; Kowalczyk, P. CO_2—Reinforced nanoporous carbon potential energy field during CO_2/CH_4 mixture adsorption. A comprehensive volumetric, in-situ IR, and thermodynamic insight. *Carbon* **2017**, *122*, 185–193. [CrossRef]
16. Jusoh, N.; Yeong, Y.F.; Lau, K.K.; Azmi, M.S. Fabrication of silanated zeolite T/6FDA-durene composite membranes for CO_2/CH_4 separation. *J. Clean Prod.* **2017**, *166*, 1043–1058. [CrossRef]
17. Venna, S.R.; Carreon, M.A. Metal organic framework membranes for carbon dioxide separation. *Chem. Eng. Sci.* **2015**, *124*, 3–19. [CrossRef]
18. Kayal, S.; Chakraborty, A. Activated carbon (type Maxsorb-III) and MIL-101(Cr) metal organic framework based composite adsorbent for higher CH_4 storage and CO_2 capture. *Chem. Eng. J.* **2018**, *334*, 780–788. [CrossRef]
19. Bello, G.; García, R.; Arriagada, R.; Sepúlveda-Escribano, A.; Rodriguez-Reinoso, F. Carbon molecular sieves from Eucalyptus globulus charcoal. *Microporous Mesoporous Mater.* **2002**, *56*, 139–145. [CrossRef]
20. Arriagada, R.; Bello, G.; García, R.; Rodriguez-Reinoso, F. Carbon molecular sieves from hardwood carbon pellets. The influence of carbonization temperature in gas separation properties. *Microporous Mesoporous Mater.* **2005**, *81*, 161–167. [CrossRef]
21. Lutyński, M.; Waszczuk, P.; Słomski, P.; Szczepańsk, J. CO_2 sorption of Pomeranian gas bearing shales—The effect of clay minerals. *Energy Procedia* **2017**, *125*, 457–466. [CrossRef]
22. Awadallah, F.A.; Al-Muhtaseb, S.A. Carbon dioxide sequestration and methane removal from exhaust gases using resorcinol–formaldehyde activated carbon xerogel. *Adsorption* **2013**, *19*, 967–977. [CrossRef]
23. Yu, H.; Zhou, L.; Cheng, J.; Hu, Q. Predictions of the adsorption equilibrium of methane/carbon dioxide binary gas on coals using Langmuir and Ideal Adsorbed Solution. *Int. J. Coal Geol.* **2008**, *73*, 115–129. [CrossRef]
24. Awadallah, F.A.; Al-Muhtaseb, S.A. Selective adsorption of carbon dioxide, methane and nitrogen using resorcinol-formaldehyde xerogel activated carbon. *Adsorption* **2017**, *23*, 933–944. [CrossRef]
25. Shen, Y.; Bai, J. A new kind CO_2/CH_4 separation material: Open ended nitrogen doped carbon nanotubes formed by direct pyrolysis of metal organic frameworks. *Chem. Commun.* **2010**, *46*, 1308–1310. [CrossRef]
26. Fonseca, A.; Reijerkerk, S.; Potreck, J.; Nijmeijer, K.; Mekhalif, Z.; Delhalle, J. Very short functionalized carbon nanotubes for membrane applications. *Desalination* **2010**, *250*, 1150–1154. [CrossRef]
27. Saito, Y.; Dresselhause, G.; Dresselhause, M.S. *Physical Properties of Carbon Nanotubes*; Imperial College Press: London, UK, 1998.
28. Pérez-Caballero, F.; Anna-Liisa, P.; Koel, M. Preparation of nanostructured carbon materials. *Proc. Est. Acad. Sci.* **2008**, *57*, 48–53. [CrossRef]
29. Wang, X.; Lu, L.-L.; Yu, Z.-L.; Xu, X.-W.; Zheng, Y.-R.; Yu, S.-H. Scalable template synthesis of resorcinol–formaldehyde/graphene gxide composite aerogels with tunable densities and mechanical propertie. *Angew. Chem. Int. Ed.* **2015**, *54*, 2397–2401. [CrossRef]
30. ElKhatat, A.M.; Al-Muhtaseb, S.A. Advances in tailoring resorcinol-formaldehyde organic and carbon gels. *Adv. Mater.* **2011**, *23*, 2887–2903. [CrossRef]
31. Xu, C.; Ruan, C.-Q.; Li, Y.; Lindh, J.; Strømme, M. High-performance activated carbons synthesized from nanocellulose for CO_2 capture and extremely selective removal of volatile organic compounds. *Adv. Sustain. Syst.* **2018**, *2*, 1700147. [CrossRef]
32. Awadallah, F.A.; Al-Muhtaseb, S.A. Nanofeatures of resorcinol–formaldehyde carbon microspheres. *Mater. Lett.* **2012**, *87*, 31–34. [CrossRef]
33. Langmuir, I. The Adsorption of gases on plane surfaces of glass, mica and platinum. *J. Am. Chem. Soc.* **1918**, *40*, 1361–1403. [CrossRef]
34. Ruthven, D.M. *Principles of Adsorption and Adsorption Processes*; John Wiley & Sons: Hoboken, NJ, USA, 1984; pp. 467–524.
35. Myers, A.L. Activity coefficients of micture adsorbed on heterogenous surfaces. *ALChE J.* **1983**, *29*, 691–693. [CrossRef]
36. Schell, J.; Casas, N.; Pini, R.; Mazzotti, M. Pure and binary adsorption of CO_2, H_2, and N_2 on activated carbon. *Adsorption* **2012**, *18*, 49–65. [CrossRef]

37. Zhou, L.; Fang, S.; Tang, J.; Gao, L.; Yang, J. Synthesis and characterization of multiwalled carbon nanotube/polyurethane composites via surface modification multiwalled carbon nanotubes using silane coupling agent. *Polym. Compos.* **2012**, *33*, 1867–1873. [CrossRef]
38. Fraczek-Szczypta, A.; Menaszek, E.; Syeda, T.B.; Misra, A.; Alavijeh, M.; Adu, J.; Blazewicz, S. Effect of MWCNT surface and chemical modification on in vitro cellular response. *J. Nanopart. Res.* **2012**, *14*, 1181. [CrossRef]
39. Tsai, W.; Yang, J.; Lai, C.; Cheng, Y.H.; Lin, C.C.; Yeh, C.W. Characterization and adsorption properties of eggshells and eggshell membrane. *Bioresour. Technol.* **2006**, *97*, 488–493. [CrossRef]
40. Everett, D.H.; IUPAC. Manual of symbol and terminology for physico -chemical quantities and units, appendix, definitions, terminology and symbols in colloid and surface chemistry, Part I. *Pure Appl. Chem.* **1972**, *31*, 579. [CrossRef]
41. Kruk, M.; Jaroniec, M.; Ryoo, R.; Joo, S.H. Characterization of MCM-48 silicas with tailored pore sizes synthesized via a highly efficient procedure. *Chem. Mater.* **2001**, *13*, 3169–3183. [CrossRef]
42. Sing, K.S.W.; Everett, D.H.; Haul, R.A.W.; Moscou, L.; Pierotti, R.A.; Rouquerol, J.; Siemieniewska, T. Reporting physisorption data for gas/solid systems with special reference to the determination of surface area and porosity. *Pure Appl. Chem.* **1985**, *57*, 603–619. [CrossRef]
43. Guan, Q.Z.; Dong, D.Z.; Wang, S.F.; Huang, J.; Wang, Y.; Hui, L.; Zhang, C. Preliminary study on shale gas microreservoir characteristics of the Lower Silurian Longmaxi Formation in the southern Sichuan Basin, China. *J. Nat. Gas Sci. Eng.* **2016**, *31*, 382–395. [CrossRef]
44. Groen, J.J.; Peffer, L.A.A. Pore size determination in modified micro- and mesoporous materials. Pitfalls and limitations in gas adsorption data analysis. *Micropor. Mesopor. Mater.* **2003**, *60*, 1–17. [CrossRef]
45. Atchudan, R.; Pandurangan, A.; Jool, J. Effects of nanofillers on the thermo-mechanical properties and chemical resistivity of epoxy nanocomposites. *J. Nanosci. Nanotechnol.* **2015**, *15*, 4255–4267. [CrossRef] [PubMed]
46. Heuchel, M.; Daviesm, G.M.; Buss, E.; Seaton, N.A. Adsorption of carbon dioxide and methane and their mixtures on an activated Carbon: simulation and experiment. *Langmuir* **1999**, *15*, 8695–8705. [CrossRef]
47. Keren, O.; Twala, N.; Oluwasina, O.; Daramola, M.O. Synthesis and performance evaluation of chitosan/carbon nanotube (chitosan/MWCNT) composite adsorbent for post-combustion carbon dioxide capture. *Energy Procedia* **2017**, *114*, 2330–2335.
48. Ngoy, J.; Wagner, N.; Riboldi, L.; Bolland, O. A CO2 capture technology using multi-walled carbon nanotubes. *Energy Procedia* **2014**, *63*, 2230–2248. [CrossRef]
49. Su, F.; Lu, C.; Chen, H.-S. Adsorption, desorption, and thermodynamic studies of CO_2 with high-amine-loaded multiwalled carbon nanotubes. *Langmuir* **2011**, *27*, 8090–8098. [CrossRef]
50. Romero, J.R.G.; Moreno-Piraján, J.C.; Gutierrez, L.G. Kinetic and equilibrium study of the adsorption of CO_2 in ultramicropores of resorcinol-formaldehyde aerogels obtained in acidic and basic medium. *C—J. Carbon Res.* **2018**, *4*, 52.
51. Xia, Y.; Yang, Z.; Zhu, Y. Porous carbon-based materials for hydrogen storage: Advancement and challenges. *J. Mater. Chem. A* **2013**, *1*, 9365–9381. [CrossRef]
52. Marco-Lozar, J.P.; Kunowsky, M.; Suárez-García, F.; Carruthersb, J.D.; Linares-Solano, A. Activated carbon monoliths for gas storage at room temperature. *Energy Environ. Sci.* **2012**, *5*, 9833–9842. [CrossRef]
53. Gu, M.; Xian, X.; Duan, S.; Du, X. Influences of the composition and pore structure of a shale on its selective adsorption of CO_2 over CH_4. *J. Nat. Gas. Sci. Eng.* **2017**, *46*, 296–306. [CrossRef]
54. Yang, H.; Gong, M.; Chen, Y. Preparation of activated carbons and their adsorption properties for greenhouse gases: CH_4 and CO_2. *J. Nat. Gas Chem.* **2011**, *20*, 460–464. [CrossRef]
55. Moon, S.H.; Shim, J.W. A novel process for CO_2/CH_4 gas separation on activated carbon fibers—Electric swing adsorption. *J. Colloid Interface Sci.* **2006**, *298*, 523–528. [CrossRef]
56. Bacsik, Z.; Cheung, O.; Vasiliev, P.; Hedin, N. Selective separation of CO_2 and CH_4 for biogas upgrading on zeolite NaKA and SAPO-56. *Appl. Energy* **2016**, *162*, 613–621. [CrossRef]
57. Rattanaphan, S.; Rungrotmongkol, T.; Kongsune, P. Biogas improving by adsorption of CO_2 on modified waste tea activated carbon. *Renew. Energy* **2010**, *145*, 622–631. [CrossRef]
58. Wu, X.-X.; Zhang, C.-Y.; Tian, Z.-W.; Cai, J.-J. Large-surface-area carbons derived from lotus stem waste for efficient CO_2 capture. *New Carbon Mater.* **2018**, *33*, 252–261. [CrossRef]
59. Siqueira, R.F.; Freitasa, R.F.; Peixotoa, H.R.; Nascimento, D.J.F.; Musse, A.P.S.; Torres, A.E.B.; Azevedo, D.C.S.; Bastos-Neto, M. Carbon dioxide capture by pressure swing adsorption. *Energy Procedia* **2017**, *114*, 2182–2192. [CrossRef]
60. Buss, E. Gravimetric measurement of binary gas adsorption equilibria of methane-carbon dioxide mixtures on activated carbon. *Gas Sep. Purif.* **1995**, *9*, 189–197. [CrossRef]
61. Rezvani, H.; Fatemi, S.; Tamnanloo, J. Activated carbon surface modification by catalytic chemical vapor deposition of natural gas for enhancing adsorption of greenhouse gases. *J. Environ. Chem. Eng.* **2019**, *7*, 103085. [CrossRef]
62. Koonaphapdeelert, S.; Moran, J.; Aggarangsi, P.; Asira, B. Low pressure biomethane gas adsorption by activated carbon. *Energy Sustain. Dev.* **2018**, *43*, 196–202. [CrossRef]
63. Awadallah, F.A.; Al-Muhtaseb, S.A. Effect of gas templating of resorcinol-formaldehyde xerogels on characteristics and performances of subsequent activated carbons. *Mater. Chem. Phys.* **2019**, *34*, 361–368. [CrossRef]

64. Wang, X.; French, J.; Kandadai, S.; Chua, H.T. Adsorption measurements of methane on activated carbon in the temperature range (281 to 343) K and pressures to 1.2 MPa. *J. Chem. Eng. Data* **2010**, *55*, 2700–2706. [CrossRef]
65. Wang, Q.; Huang, L. Molecular insight into competitive adsorption of methane and carbon dioxide in montmorillonite: Effect of clay structure and water content. *Fuel* **2019**, *239*, 32–43. [CrossRef]